Rigidity Criteria for Chainmail Consisting of Tessellations of Torus Knots

Hujie Yan,[1,*] Zhiqiang Meng,[2,*] Ziran Zhou,[1] Wenjie Zhou,[1,†] and Chiara Daraio[1,‡]
[1]Division of Engineering and Applied Science, California Institute of Technology, Pasadena, California 91125, USA
[2]School of Mechanical Engineering and Aerospace Engineering, Nanyang Technological University, Singapore

(Received 31 January 2025; accepted 18 June 2025; published 22 August 2025)

Interlocked and polycatenated material systems, consisting of discrete, nonconvex particles linked to their nearest neighbors, such as chainmail fabrics, have been shown to undergo a jamming transition that increases their rigidity under boundary compression. This rigidity transition is associated with an increase in contact number between particles. In architected materials, rigidity is described by theories such as the Maxwell criterion. In this Letter, we propose a rigidity theory for a type of interlocked material system: the torus knot tessellation. Torus knot tessellations are structured fabrics composed of particles shaped as torus knots. In these fabrics, we theoretically demonstrate that in-plane rigidity is governed by a modified Maxwell criterion, while out-of-plane rigidity is governed by a crease line criterion. These theories provide a framework for the design of rigidity of these fabrics.

DOI: 10.1103/q4k4-x2zm

The design of material structure has emerged as a powerful strategy for controlling the mechanical response of engineered systems, offering far greater flexibility than traditional synthesis of composites and foams [1,2]. This design paradigm enables the creation of architected materials with tailored and extraordinary properties, such as negative Poisson's ratio [3,4], reversible deformation [5], ultralight yet ultrastiff response [6,7], multimodal deformations [8–10], and logic ability [11,12]. Structured fabrics with interlocked particles, like chainmail, have historically been used in wearable protective armor [13–15]. Recently, these materials have been shown to support a jamming transition that converts them from flexible fabrics to rigid layers upon the application of external pressure [16]. Some of the unique characteristics of chainmail fabrics arise from the discrete nature of their components: nonconvex granular particles that are topologically interlocked with one another.

Conventional granular matter, such as sand or grain piles, consists of densely packed, disordered particles that can jam under applied external pressure [17–20]. The behavior of these materials is governed by the particles' geometry [21,22], surface roughness [23,24], moisture content [25,26], etc. The mechanical stability of granular matter is determined by compressive contacts between adjacent elements, which transmit stresses along preferential pathways known as "force chains" [27,28].

In interlocked granular matter, the particles are arranged in ordered lattices and interlocked together, supporting both compressive and tensile interactions that maintain the integrity of the entire structure [29]. Interlocked fabrics have found applications in soft robotics [30,31] and biomedical devices [32,33], owing to their flexibility and tunable stiffness. The jamming transition observed in interlocked granular matter depends on the interparticle connectivity (i.e., how particles are topologically interlocked). This connectivity influences how force chains propagate through particle contacts, thereby affecting the overall mechanical properties [20].

Here, we aim to propose a rigidity theory that uses connectivity to assess whether a structure can be forced out of shape without elastic deformation for single-layer fabrics of interlocked granular matter. We focus on chainmail fabrics consisting of particles derived from torus knots, tessellated into a 2D fabric, termed torus knot tessellation (TKT). We chose torus knot-shaped particles to have direct control of the connectivity between nearest neighbor particles. We introduce a general design method for creating fabrics from interlocked torus knot particles and analyze the particles' connectivity using a point-bar model. We then derive rigidity criteria to predict rigidity of in-plane deformation and out-of-plane folding. Our findings reveal that TKT fabrics with varying connectivity exhibit remarkably different reactions to external forces. Finally, we demonstrate how to apply these theories to design the rigidity of these fabrics.

The fundamental building blocks of TKT are torus knot particles [Fig. 1(a)]. A torus knot is a mathematical curve with zero thickness that coils around the surface of a torus. To transform this curve into a particle, we assign a circular

*These authors contributed equally to this work.
†Contact author: zhouw@caltech.edu
‡Contact author: daraio@caltech.edu

cross section to it. Mathematically, a torus knot can be described as

$$\begin{cases} x = [R + r\cos(qt)]\cos(pt) \\ y = [R + r\cos(qt)]\sin(pt) \\ z = r\sin(qt) \end{cases} \quad (1)$$

Here, t is the parameter governing the formation of the curve and ranges from 0 to 2π, R and r determine the dimensions of the torus knot, p defines the topology and is set to 1 throughout the study, and q determines the number of "petals" of the torus knot (i.e., loop features surrounding the original torus). For instance, in Fig. 1(a), a torus knot particle is generated around a torus with $q = 3$. More generally, the orientations and lengths of the petals can be adjusted by modifying the original formula, as detailed in Supplemental Material (SM) [34], Sec. 1.

A torus knot particle can be represented by a point-bar diagram [Fig. 1(b), where hollow blue points represent the particles' centers, and solid orange points represent the ends of the particles' petals]. Adjacent particles can be further interlocked into fabrics [Figs. 1(c) and 1(d)]. Note that in connecting the torus knot particles, all the particles remain in the same plane instead of rotating alternately with each other like the traditional chain structure. The proposed design pipeline enables us to define numerous TKTs (see SM [34], Sec. 2).

Because of the discrete nature of these fabrics, any fabric deformation can be decomposed into two parts: the deformation allowed by interparticle clearance (clearance deformation) and the deformation allowed by the mechanism from the specific structure (structural deformation).

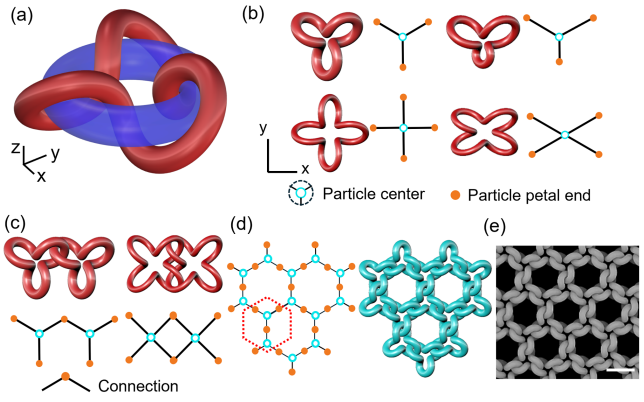

FIG. 1. Schematic diagram to represent the design of a TKT. (a) A rod coils around a base torus (blue) for one revolution and forms a torus knot particle (red). (b) Top view of the torus knot particles and their point-bar representations. (c) Particles can be interlocked by hooking at the connections. (d) A TKT fabric is generated by repeating the connection process, following a 2D tessellation. A representative periodic cell is isolated in red dashed line. Note that an effective periodic cell may span multiple geometrical unit cells, as in Ref. [35]. (e) Digital photo (false color used for clarity) of a 3D printed TKT fabric. Scale bar, 1 cm.

To determine the effect of connectivity on the rigidity of these fabrics, it is crucial to limit clearance deformation, as it is irrelevant to the structures of the fabrics. Thus, in designing, we ensure as minimal clearance as possible (the clearance is smaller than 5% of the particle wire thickness, which is much smaller than the scale of the particle). We also assume perfectly smooth surfaces to avoid the factor of surface conditions. With these constraints, the connections between particles function similarly to ball hinges: translational movements are limited within the range of the clearance, while rotational movements are not limited. Thus, we model the connection in Fig. 1(c) as a single orange point. Note that beyond TKTs, the above assumptions can be applied to some other interlocked structures as well; see SM [34], Sec. 9.

We compare in-plane rigidity of two distinct TKTs [bilink and trilink, Figs. 2(a) and 2(c); see SM [34] Fig. 4S for structural details]. We apply uniform compression to deform the fabrics until elastic deformation occurs. Their experimental responses are compared in Figs. 2(b) and 2(d), respectively. We observe that trilink only has a small clearance deformation, while bilink has a much larger structural deformation beyond clearance deformation. As a quantitative comparison of their difference, the area shrinkage (Γ) of the trilink is much less than that of the bilink. We compare these experimental results with numerical simulations (Fig. S6) obtained with the level-set discrete element method [36–38], finding good agreement. The implementation details of the level-set discrete element method can be found in SM [34], Sec. 5.

The difference of rigidity in these two fabrics arises from the particles' rigid body interactions. In truss or lattice frameworks, Maxwell's criterion is usually effective for determining rigidity by counting degrees of freedom (DOFs) in the system [39,40]. Grubler's criterion further extends the object to a system composed of arbitrary rigid bodies [41] at the cost of losing geometry information (e.g., shapes of rigid bodies, interlocking patterns, periodicity). To conserve geometric information in our TKT fabrics, we adapt Maxwell's criterion for predicting rigidity. We draw an analogy between TKTs and 2D truss systems in the context of Maxwell's criterion. Truss systems consist of joints and bars. According to Maxwell's criterion, the rigidity of these systems depends on the number of total DOFs, which can be evaluated by counting the number of joints (j) and bars (b) in the entire system. Each joint has two DOFs (x and y translations) and each bar introduces a geometric constraint on two joints that forbids axial bar deformation. In addition, the three overall rigid-body DOFs should be excluded. The resulting Maxwell criterion formula [42] is $M = 2j - b - 3$. For $M > 0$, the system has extra DOFs and behaves in-plane flexible. Conversely, for $M \leq 0$, the system is in-plane rigid.

We expand this analysis to our TKT fabrics. In their point-bar diagrams [Figs. 1(b)–1(d)], each point (both blue

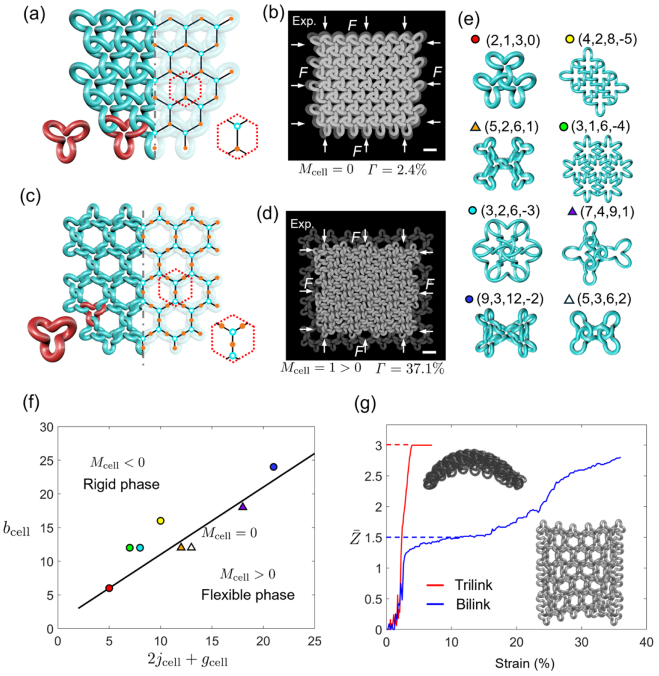

FIG. 2. In-plane response of TKT fabrics. (a),(c) Three-petal particles tessellated with different connectivity. In (a), groups of three neighboring particles are interlocked (termed "trilink"), whereas in (c), interlocking occurs between pairs of particles (termed "bilink"). Their respective periodic cells are represented in hexagonal dashed lines. (b),(d) Digital photos (in false color) of the two fabrics responding to uniform in-plane compression. Γ represents the ratio of area shrinkage after deformation. Scale bars, 1 cm. (e) Eight TKT fabrics are selected based on a diversity of petal number, petal orientation and interlocking topology (See SM [34], Sec. 4 for details). Experimental and numerical results are obtained and used to divide them into a rigid group (circular markers) and a flexible group (triangular markers). The counting values of these TKTs are listed in the order (j, g, b M). (f) Each TKT cell is counted and mapped to a colored point in a 2D phase diagram. The modified Maxwell's criterion is verified through our observation that the rigid group is distributed above the $M_{\text{cell}} = 0$ plane, while the flexible group is distributed below the plane. (g) The two profiles of average contact number ($\bar{Z}$) versus compressive strain. The minimum contact number (Z^*) is indicated by dashed lines.

and orange) has two translational DOFs, akin to the truss. However, we identify two differences in TKTs: (i) every blue point has an additional rotational DOF, counting the orientation of each rigid body; (ii) each bar contributes two constraints, since in a rigid body both axial and transverse deformations in the bars are forbidden. Therefore, the modified Maxwell criterion gives $M = 2j + g - 2b - 3$ [Eq. (2)], where g indicates the number of particles. This criterion has not considered geometrical information like periodicity.

For TKTs with periodic patterns, the rigidity criterion can be further simplified. First, we make the naïve assumption that each periodic cell has identical distortion. Thus, the point movements are the same across all cells. Consequently, the DOFs of the entire structure are effectively those in a single cell, counted as $2j_{cell} + g_{\text{cell}}$. Similarly, the strains in bars are consistent across all cells, resulting in a total constraint number b_{cell}. For overall DOFs, we reduce three rigid-body DOFs. Another four DOFs must be added for the following reason: to tile a 2D space with periodic cells, we need to specify two lattice vectors, each of which requires two parameters (length and direction). Therefore, the modified Maxwell's criterion for periodic TKT fabrics is

$$M_{\text{cell}} = 2j_{\text{cell}} + g_{\text{cell}} - 2b_{\text{cell}} + 1 \tag{2}$$

If $M_{\text{cell}} > 0$, the system is in-plane flexible. Conversely, if $M_{\text{cell}} \leq 0$, the system is in-plane rigid.

As an example, we explain the results in Figs. 2(b) and 2(d). The trilink cell has $j_{\text{cell}} = 2$, $g_{\text{cell}} = 1$, $b_{\text{cell}} = 3$, and $M_{\text{cell}} = 0$, leading to a rigid behavior. As a comparison, the bilink cell has $j_{\text{cell}} = 5$, $g_{\text{cell}} = 2$, $b_{\text{cell}} = 6$, resulting in an $M_{\text{cell}} = 1$. Therefore, the structure exhibits flexibility. These predictions are consistent with our experiments and simulations. To test the criterion's generality, we tested in-plane rigidity on eight TKT fabrics [Fig. 2(e) and SM [34], Sec. 6]. A phase diagram differentiating rigidity and flexibility is plotted accordingly [Fig. 2(f)]. This phase diagram clearly shows the effectiveness of the proposed rigidity criterion.

Note that this criterion can also be derived from a more mathematically rigorous method that involves setting up a matrix of geometric constraints and solving for zero-energy modes [43]. When the matrix has dependent rows (meaning dependent geometric constraints) or gives nonperiodic solution in null space (i.e., aperiodic zero-energy modes), the Maxwell criterion may break down, as detailed in SM [34], Sec. S3.

We note that the in-plane rigidity criterion is consistent with the contact number argument provided in previous works [16,29]. In Fig. 2(g), we plot the average contact number ($\bar{Z}$) of each particle against compressive strain. The minimum contact number (Z^*) is defined as the value of $\bar{Z}$ when the structures start to jam, which can be calculated by counting the number of connection pairs around a particle (3 for trilink and 1.5 for bilink). As $\bar{Z}$ reaches Z^*, trilink cannot be further compressed in the plane and shows out-of-plane buckling, while bilink continues to distort in the plane as it has DOFs that allow further contraction.

We then study the relation between out-of-plane rigidity and tessellation patterns. To maintain consistency of tessellation patterns, we focus on TKT fabrics with $M_{\text{cell}} < 0$, as they do not produce in-plane structural deformation. Let us consider, as an example, the two TKT fabrics in Figs. 3(a) and 3(d) (named four-petal and six-petal, respectively). Experimentally, we test their folding rigidity by partially suspending the fabrics from the edge of a plane. In Fig. 3(b), the four-petal folds, whereas

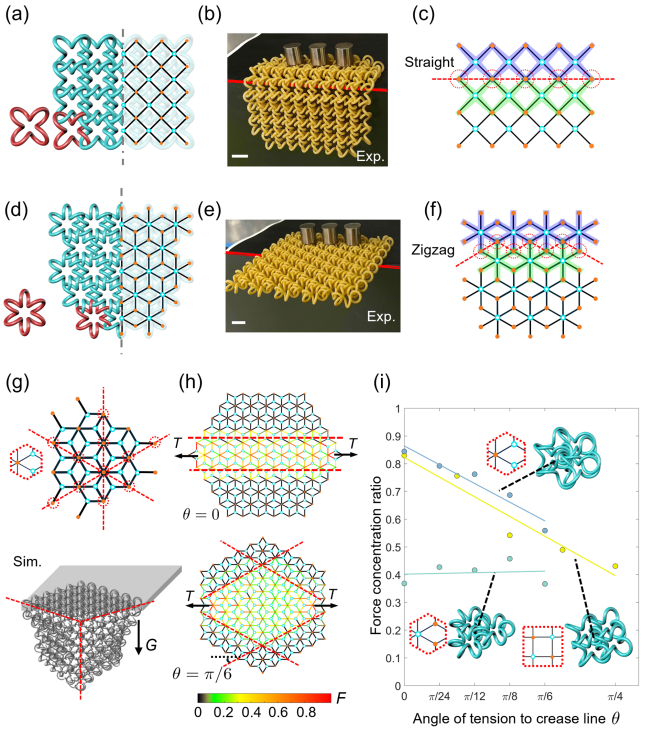

FIG. 3. Folding rigidity and force chain analysis of TKT fabrics. Distinct folding behaviors are observed in (a) four-petal and (d) six-petal. When partially suspended from the edge of a plane, (b) four-petal folds, (e) while six-petal does not fold. The corresponding point-bar representations are shown in (c) and (f). We focus on two arrays of particles (highlighted by purple and green regions). The connections between the arrays are marked by circles, and the red dashed line connecting them represents either a straight crease line or a geometric constraint in a zigzag pattern. (g) Three-petal, a TKT with three crease lines. The fabric folds along three crease lines, forming a kink at their conjunction. (h) Visualized force chain networks of the three-petal when a pair of tension forces is applied along the central axis. The color map represents the force magnitude, normalized to the range between 0 and 1. The fabric is rotated 30° to change the direction of crease lines. (i) The plot of force concentration ratio (FCR) against θ. Each point represents one test result of angle θ and its corresponding FCR. The lines are the fitted trends of FCR when θ increases. Scale bars, 2 cm.

the six-petal remains rigid, as seen in Fig. 3(e). To intuitively explain this difference, we focus on two adjacent arrays along the folding direction [Figs. 3(c) and 3(f)]. The folding rigidity depends on whether these two arrays can rotate relative to one another, a factor directly related to the connectivity between them. In Fig. 3(c), the connections are aligned into a crease line.

This allows these points to effectively function as a hinge or a crease. In Fig. 3(f), the connections form a zigzag pattern, which functions as a geometric constraint that prohibits folding.

To demonstrate the effectiveness of this crease-line criterion, we conduct folding tests on other TKT fabrics as well (see SM [34], Sec. 7 for details). The nontrivial directed folding behavior of a fabric (named three-petal) is shown in Fig. 3(g). This result shows that in TKTs folding directions tend to align with one of the crease lines.

The effectiveness of the crease-line criterion reflects how interlocking topology affects force chain propagation. Like conventional granular matter, when external forces are applied, a network of force chains forms within the TKT through contacts between neighboring particles. During folding tests of certain TKT fabrics [e.g., Fig. 3(e)], the hanging part of TKT fabrics does not drape because the support forces are transmitted here through force chains. This force chain network arises from the topological interlocking of TKTs and should be observable in planar tension tests where particles engage with each other. Figure 3(h) visualizes the force chains on the three-petal fabric with different orientations, which show the tendency to spread parallel to the crease lines. This is because a particle array along a crease line is not geometrically constrained by the neighboring parallel arrays.

To quantitatively study the relation between the force chain spreading and the crease line orientation, we define a force concentration ratio (FCR) as

$$FCR = 1/\frac{\sum_i F_i y_i}{\sum_i F_i a} \tag{3}$$

Here, i sums over all the petals in the TKT fabric and y_i is the vertical distance from the i th petal to the central axis. The term $\sum_i F_i y_i / \sum_i F_i$ represents the weighted average distance of the force chain network, and a is the petal length as the normalization factor. An FCR value close to 1 indicates force concentration near the point of application, whereas a value close to 0 signifies a strong force dispersion across the structure.

We keep the tensile force in the horizontal direction and change the orientation of the fabrics. We choose, θ the angle between the horizontal axis and the crease line, as the measure of fabric orientation. Figure 3(i) displays the FCR values against the orientation of the fabrics. For the three-petal and the four-petal, which have well-defined crease lines, the FCR is highest when the tension aligns with the crease line ($\theta = 0$). As θ increases, the FCR drops, indicating the effect of force chain spreading. For the six-petal, which lacks a crease line, θ is defined as the rotation angle from an arbitrary direction. The FCR nearly keeps unchanged in this case because of its lack of a crease line as a force chain guide. This result highlights the potential of leveraging interlocking topology and crease lines in TKT fabrics to achieve force chain programming.

We exemplify two methods to adjust the TKT's rigidity: (i) we can change the DOFs by locally controlling the connections between particles, thereby switching the in-plane rigidity; (ii) we can change the position of crease lines through the reorientation of TKT fabrics, thus tuning the folding rigidity.

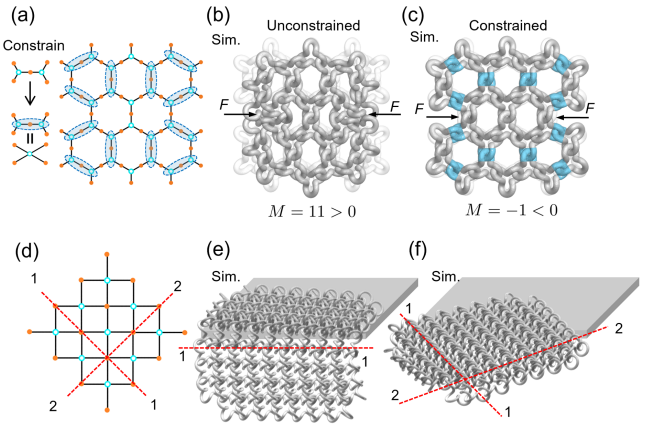

FIG. 4. Designing the rigidity of TKT fabrics. (a) Point-bar representation of a TKT fabric. The blue regions are to be constrained to switch this fabric into a rigid one. (b) The fabric is flexible when a pair of pointwise force is applied. (c) When the specified constraints are applied, the fabric becomes in-plane rigid. (d) The point-bar representation of a TKT fabric that has two perpendicular crease lines in red. (e) The initial orientation gives a flexible folding behavior, while (f) a 45° rotation reorients the crease lines and makes the fabric rigid.

We first construct an in-plane flexible TKT fabric [Fig. 4(b)]. We aim to make this fabric rigid by constraining a certain number of connections. This number is given by the modified Maxwell's criterion, $M = 11$ in this case. In consideration of symmetry, we specify 12 connections in Fig. 4(a). Each constraint combines two discrete particles into a whole, reducing the DOFs by 1. The resulting fabric becomes rigid, as shown in Fig. 4(c).

For designing the folding rigidity, we start with the fabric in Fig. 4(d), where the two perpendicular crease lines exist. When folding along one of the lines, as in Fig. 4(e), the fabric is flexible. Then, we reorient the fabric to misalign the crease lines and the folding direction. The fabric behaves rigidly in this new direction [Fig. 4(f)]. This intriguing anisotropy of folding properties enables a fast and simple design approach of folding rigidity.

In summary, our research has led to the creation and demonstration of a new category of interlocked granular matter, characterized by torus knot tessellation (TKT). In this approach, particles shaped as torus knots are interlocked following specific tessellation patterns. The various choices of tessellation patterns and particle shapes allow great variability in fabric design possibilities.

We propose rigidity criteria for both in-plane deformation and out-of-plane folding behaviors in these fabrics. By comparing TKT fabrics with a 2D truss, a modified Maxwell criterion is derived for nonperiodic deformations. We further simplify our criterion with the periodic assumption, which successfully predicts in-plane rigidity of the TKT fabrics. For folding rigidity, we unveil a crease-line criterion and investigate the corresponding force chain network. The generality of both criteria is verified through experiments and simulations. Finally, we demonstrate how these criteria can be applied to design the structure's rigidity. The design framework and findings presented in this study are applicable to fields such as soft robotics, biomedical devices, and aerospace architectures, enabling the creation of shape morphing surfaces, conformable exoskeletons, and deployable structures.

Acknowledgments—This research has been supported by the National Science Foundation (Grant No. 2242925) and the Multi University Research Initiative (Grant No. MURI ARO W911NF-22-2-0109). We thank Prof. José E. Andrade's group for their initial implementation of the LSDEM simulation.

Data availability—The data supporting this study's findings are available within the Letter.

[1] K. Bertoldi, V. Vitelli, J. Christensen, and M. van Hecke, Nat. Rev. Mater. **2**, 17066 (2017).
[2] M. Kadic, G. W. Milton, M. van Hecke, and M. Wegener, Nat. Rev. Phys. **1**, 198 (2019).
[3] A. Clausen, F. Wang, J. S. Jensen, O. Sigmund, and J. A. Lewis, Adv. Mater. **27**, 5523 (2015).
[4] A. Rafsanjani and D. Pasini, Extreme Mech. Lett. **9**, 291 (2016).
[5] S. Shan, S. H. Kang, J. R. Raney, P. Wang, L. Fang, F. Candido, J. A. Lewis, and K. Bertoldi, Adv. Mater. **27**, 4296 (2015).
[6] X. Zheng *et al.*, Science **344**, 1373 (2014).
[7] X. Zhang, A. Vyatskikh, H. Gao, J. R. Greer, and X. Li, Proc. Natl. Acad. Sci. U.S.A. **116**, 6665 (2019).
[8] J. T. Overvelde, J. C. Weaver, C. Hoberman, and K. Bertoldi, Nature (London) **541**, 347 (2017).
[9] C. Coulais, A. Sabbadini, F. Vink, and M. van Hecke, Nature (London) **561**, 512 (2018).
[10] A. Bossart, D. M. J. Dykstra, J. van der Laan, and C. Coulais, Proc. Natl. Acad. Sci. U.S.A. **118**, e2018610118 (2021).
[11] T. Chen, O. R. Bilal, K. Shea, and C. Daraio, Proc. Natl. Acad. Sci. U.S.A. **115**, 5698 (2018).
[12] L. J. Kwakernaak and M. van Hecke, Phys. Rev. Lett. **130**, 268204 (2023).
[13] A. R. Ploszajski, R. Jackson, M. Ransley, and M. Miodownik, MRS Adv. **4**, 1361 (2019).
[14] J. Engel and C. Liu, J. Micromech. Microeng. **17**, 551 (2007).
[15] E. Brown, A. Nasto, A. G. Athanassiadis, and H. M. Jaeger, Phys. Rev. Lett. **108**, 108302 (2012).
[16] Y. Wang, L. Li, D. Hofmann, J. E. Andrade, and C. Daraio, Nature (London) **596**, 238 (2021).
[17] H. M. Jaeger, Soft Matter **11**, 12 (2015).
[18] D. Bi, J. Zhang, B. Chakraborty, and R. P. Behringer, Nature (London) **480**, 355 (2011).
[19] A. J. Liu and S. R. Nagel, Nature (London) **396**, 21 (1998).
[20] A. J. Liu and S. R. Nagel, Annu. Rev. Condens. Matter Phys. **1**, 347 (2010).

[21] M. Gonzalez, J. Yang, C. Daraio, and M. Ortiz, Phys. Rev. E **85**, 016604 (2012).
[22] T. Pöschel and V. Buchholtz, Phys. Rev. Lett. **71**, 3963 (1993).
[23] L.-T. Sheng, W.-C. Chang, and S.-S. Hsiau, Phys. Rev. E **94**, 012903 (2016).
[24] N. A. Pohlman, B. L. Severson, J. M. Ottino, and R. M. Lueptow, Phys. Rev. E **73**, 031304 (2006).
[25] C.-J. Hsu, D. L. Johnson, R. A. Ingale, J. J. Valenza, N. Gland, and H. A. Makse, Phys. Rev. Lett. **102**, 058001 (2009).
[26] J. I. Perry, C. H. Braithwaite, N. E. Taylor, A. D. Pullen, and A. P. Jardine, Appl. Phys. Lett. **109**, 174103 (2016).
[27] L. Zhang, Y. Wang, and J. Zhang, Phys. Rev. E **89**, 012203 (2014).
[28] L. Sanfratello, E. Fukushima, and R. P. Behringer, Granular Matter **11**, 1 (2009).
[29] W. Zhou, S. Nadarajah, L. Li, A. G. Izard, H. Yan, A. K. Prachet, P. Patel, X. Xia, and C. Daraio, Science **387**, 269 (2025).
[30] Z. Hu, A. Ahmed, W. Wan, T. Watanabe, and K. Harada, in *2023 IEEE International Conference on Robotics and Automation* (IEEE, London, 2023), pp. 7405–7411.
[31] Z. Xie, M. Mohanakrishnan, P. Wang, J. Liu, W. Xin, Z. Tang, L. Wen, and C. Laschi, IEEE Rob. Autom. Lett. **8**, 3597 (2023).
[32] Y. Tian *et al.*, Adv. Sci. **10**, 2301567 (2023).
[33] G. Wang, H. Wang, W. Gao, X. Yang, and Y. Wang, IEEE Robot. Autom. Lett. **8**, 3693 (2023).
[34] See Supplemental Material at http://link.aps.org/supplemental/10.1103/q4k4-x2zm for additional results, detailed derivations, design procedure, and simulation methods.
[35] K. Bertoldi, P. M. Reis, S. Willshaw, and T. Mullin, Adv. Mater. **22**, 361 (2010).
[36] P. A. Cundall and O. D. L. Strack, Géotechnique **29**, 47 (1979).
[37] R. Kawamoto, E. Andò, G. Viggiani, and J. E. Andrade, J. Mech. Phys. Solids **111**, 375 (2018).
[38] R. Kawamoto, E. Andò, G. Viggiani, and J. E. Andrade, J. Mech. Phys. Solids **91**, 1 (2016).
[39] S. Pellegrino and C. R. Calladine, Int. J. Solids Struct. **22**, 409 (1986).
[40] V. S. Deshpande, M. F. Ashby, and N. A. Fleck, Acta Mater. **49**, 1035 (2001).
[41] J. J. Uicker, G. R. Pennock, and J. E. Shigley, *Theory of Machines and Mechanisms* (Oxford University Press, New York, 2003).
[42] J. C. Maxwell, Philos. Mag. **27**, 294 (1864).
[43] S. Guest, J. Mech. Phys. Solids **51**, 383 (2003).